




TECHNICAL ARTICLE

Effect of Heat Treatment on Microstructure and Tensile Properties of Ti-6Al-4V Alloy Produced by Coaxial Electron Beam Wire Feeding Additive Manufacturing

JIANAN HU,¹ JIAHUA ZHANG,¹ YA WEI,² HAO CHEN,¹
YI YANG ^{1,5} SONGQUAN WU,¹ DMYTRO KOVALCHUK,³
ENQUAN LIANG,² XI ZHANG,² HAO WANG,^{1,6} and AIJUN HUANG⁴

1.—School of Materials Science and Engineering, University of Shanghai for Science and Technology, Shanghai 200093, China. 2.—Shanghai Aircraft Design and Research Institute, Shanghai 201210, China. 3.—JSC NVO Chervona Hvilya, Kyiv 03680, Ukraine. 4.—Department of Materials Science and Engineering, Monash University, Clayton, VIC 3800, Australia. 5.—e-mail: yiyang.imr@163.com. 6.—e-mail: haowang7@usst.edu.cn

A novel coaxial electron beam wire feeding additive manufacturing technology (CAEBWAM) was proposed in our previous work to refine the microstructure and improve the mechanical properties of titanium alloys. In the present work, different post-heat treatments were performed to understand the microstructure evolution and the resultant mechanical properties of CAEBWAMed Ti-6Al-4V alloy. The as-built sample was dominated by equiaxed prior β microstructure, with the first several deposited layers containing columnar prior β grain morphology. The as-built alloy showed a mixed microstructure composed of large α' martensite and fine $\alpha + \beta$ lamella. As the annealing temperature was increased, α' martensite decomposed into $\alpha + \beta$ phase, while the width of the α lamellae increased, causing an increase in the ductility and a decrease in the strength.

INTRODUCTION

Ti-6Al-4V has been widely used worldwide due to its excellent fatigue resistance and high strength-to-weight ratio.^{1,2} However, the conventional manufacturing approach limits the application of titanium alloys due to the low buy-to-fly ratio.^{3–7} Additive manufacturing (AM) is a rapid manufacturing technology to fabricate near-net-shape structures by adding materials in a layer-by-layer fashion.^{8–15} Depending on the feeding material, metal AM can be categorized into powder bed/feed AM and wire feeding AM.¹⁶ Among these, wire feeding AM can produce larger parts with higher deposition efficiency at relatively low cost, which is more suitable for the aerospace industry.

It has been widely understood that the mechanical properties of Ti-6Al-4V alloy fabricated by additive manufacturing are affected by its macro/

microstructure characteristics, which are sensitive to the fabrication process and post-heat treatment. As shown in previous studies,^{6,7,13,17–21} coarse columnar β grains (CG β) grow epitaxially along the $\langle 001 \rangle$ direction and result in anisotropy in the mechanical properties, i.e., outstanding strength with inferior ductility in the direction of travel, but superior ductility with low strength in the build direction. Post-heat treatment is expected to improve the mechanical properties. Heat treatment at temperatures below 550°C may result in precipitation of ordered intermetallic compound Ti₃Al with D019 structure and reduce the ductility. Heat treatment above the β transus will remove the barrier at grain boundaries and result in severe β grain growth. Thus, post-heat treatment in the $\alpha + \beta$ phase field is commonly used to release residual stress, homogenize the microstructure, and improve the mechanical properties.

Recently, a novel coaxial electron beam wire feeding additive manufacturing technology (CAEBWAM), named xBeam 3D metal printing, was

invented.²² The wire is fully enveloped by a hollow conical electron beam with a gradual distribution of energy density. Contamination caused by oxygen, nitrogen, and hydrogen can be easily prevented by using the electron beam due to the vacuum environment used. In our latest work,²³ we reported that CAEBWAMed Ti-6Al-4V alloy presented weak anisotropy and high strength and ductility. These superior tensile properties arise from a microstructure with fine equiaxed β grains (EG β), discontinuous grain boundary α (α_{GB}) phase, and short intragranular α lamellae. However, investigation on the effect of heat treatment on its microstructure and mechanical properties remains limited.

In the present work, a Ti-6Al-4V part was fabricated by CAEBWAM technology. The effects of annealing treatment at different temperatures as well as solution and aging treatments on the microstructure evolution and tensile properties were investigated.

EXPERIMENTAL PROCEDURES

The xBeam 3D metal printer used in this work consists of a hollow conical electron beam gun with a maximum power of 18 kW, a working chamber with an operating vacuum of 5×10^{-2} mbar to 5×10^{-1} mbar, an automatic wire feeder, and a three-axis numerical control working table. A schematic diagram and the machine are shown in Fig. 1a and b.^{22,23} The wire was fully surrounded by the electron beam, and consistent power was distributed between the wire and substrate, and different H are subjected to different levels of energy as shown in Fig. 1c, d.^{22,23} Ti-6Al-4V wire with diameter of 3.0 mm was used as the feedstock; the wire composition

was 6.26 wt.% Al, 4.25 wt.% V, 0.22 wt.% Fe, and 0.12 wt.% O, being deposited onto a polished hot-rolled Ti-6Al-4V substrate. The power employed was 6 kW, while the wire feeding speed and substrate travel speed were 18 mm/s and 16 mm/s, respectively. The overlap was 4 mm, and the single-layer thickness was about 1.5 mm. As-fabricated Ti-6Al-4V was subjected to a series of heat treatments, as follows: 690°C/2 h/FC to 496°C/AC (HT1), 750 °C/2 h/FC to 496°C/AC (HT2), 810°C/2 h/FC to 496°C/AC (HT3), 870°C/2 h/FC to 496°C/AC (HT4), 900°C/2 h/FC to 496°C/AC (HT5), 940°C/1 h/AC + 540°C/4 h/AC (HT6), 940°C/1 h/AC + 560°C/4 h/AC (HT7), 960°C/1 h/AC + 560°C/4 h/AC (HT8), where AC indicates air cooling and FC indicates furnace cooling. Tensile testing was carried out using an AG-5000A machine at room temperature at a strain rate of 0.005/min and 0.05/min before and after yielding, respectively, according to ASTM E8/E8M-16a. The tensile specimens were cylindrical rods with gauge diameter of 6 mm and gauge length of 24 mm. The specimens were prepared, and then etched by Kroll reagent for microstructural analysis. A Leica DMi8 optical microscope (OM) and FEI Quanta 450 FEG scanning electron microscope (SEM) were employed for microstructure observation. Phase identification was carried out by using a Bruker D8 Advance diffractometer (XRD) with a Cu K_{α} source at 40 kV and 300 mA.

RESULTS AND DISCUSSION

Microstructure of As-Built Alloy

Figure 2 shows the representative macrostructure and microstructure of Ti-6Al-4V fabricated by CAEBWAM technology in $Y-Z$ section, where X is

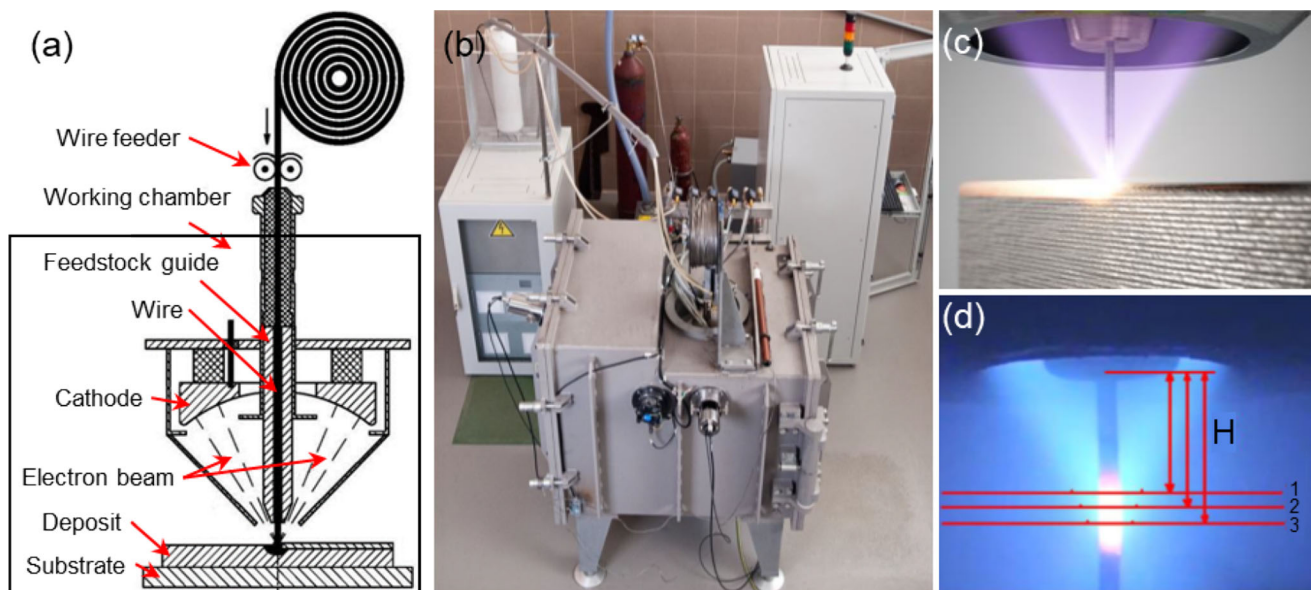


Fig. 1. (a) Schematic diagram of coaxial electron beam wire feeding additive manufacturing system; (b) xBeam 3D metal printer; (c) illustration of CAEBWAM process; (d) schematic diagram of gradually distributing energy concentration.

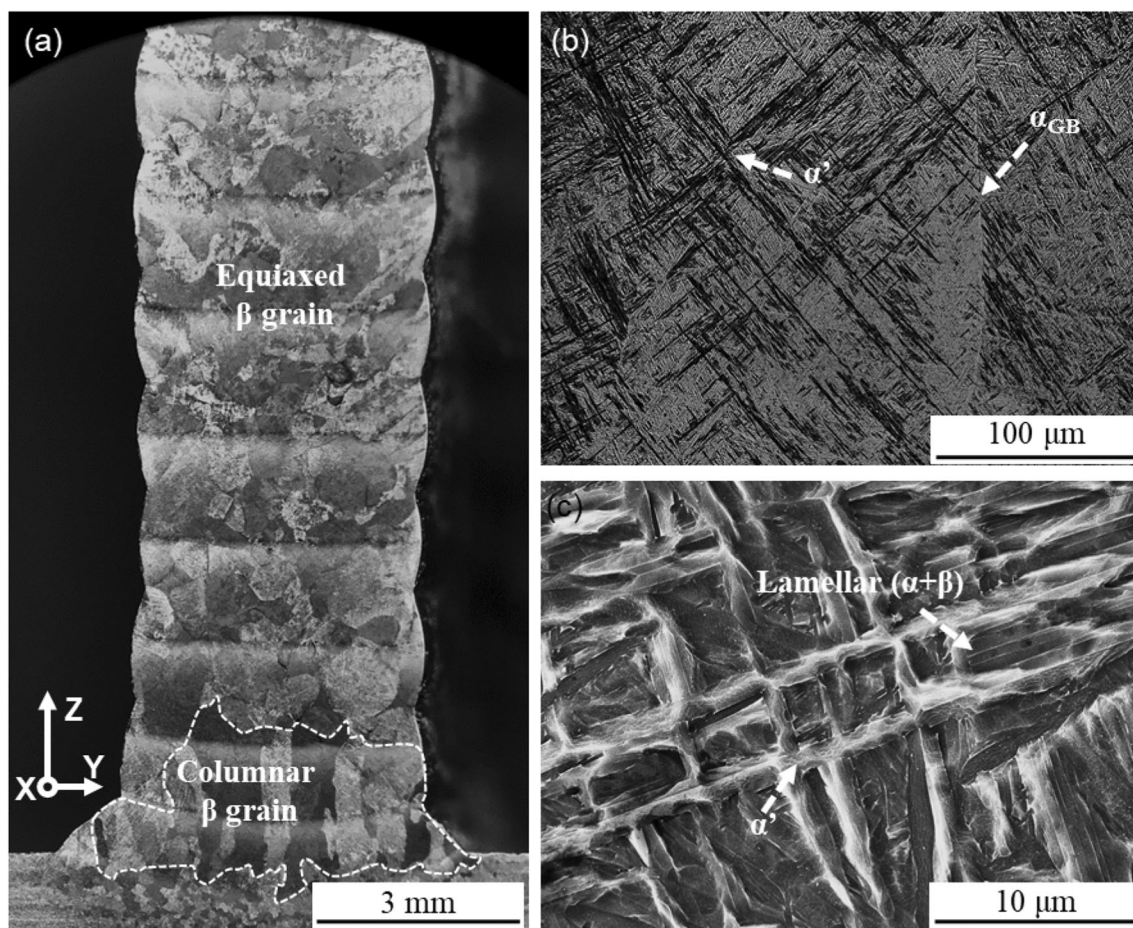


Fig. 2. (a) Optical macrograph in Y-Z section of as-built Ti-6Al-4V, where the white dashed shape shows the columnar β grain region; (b) optical microstructure of as-built Ti-6Al-4V, showing a martensitic microstructure and grain boundary α phase; (c) SEM image of as-built Ti-6Al-4V, showing α' martensite and $\alpha + \beta$ lamellar structure.

the substrate travel direction, Z is the build direction, and Y is vertical to X and Z. It can be observed that the EG β morphology is dominated and the CG β zone is mainly located in the first three layers (Fig. 2a). The dominated EG β arises from a special combination of the temperature gradient and solidification rate, as discussed in our previous work.²³ Due to the unique heat dissipation mode in the vacuum conditions, in which thermal convection is arrested, only a small fraction of the input heat is dissipated via thermal radiation while the main route for heat dissipation is via the deposited layers along the vertical direction to the substrate. Therefore, the temperature of the previously deposited layer can mostly be retained during the deposition process. In the first deposited layers, the low substrate temperature causes the molten pool to dissipate heat quickly, resulting in both temperature gradient (G) and solidification rate (R) at high levels and the formation of CG β . Because of heat accumulation and increased temperatures at higher

layers, both G and R gradually decrease during deposition, and EG β forms.

The as-built microstructure within the prior β grains in CAEBWAMed Ti-6Al-4V is different from the homogeneous acicular α' martensite seen after selective laser melting (SLM),^{13,18,24–26} and the lamellar structure observed with wire and arc additive manufacturing (WAAM) and conventional electron beam wire feeding additive manufacturing (EBWAM).^{27–29} The as-built alloy presents a mixed microstructure composed of large α' martensite and fine $\alpha + \beta$ lamella (Fig. 2b and c). The XRD profile also indicates the presence of a small amount of β phase in the as-built alloy (Fig. 3). Since the α' martensite and α phase have the same crystal structure and similar lattice parameters, only two peaks can be distinguished (α/α' peak and β peak). The formation of this unique microstructure is due to a moderate cooling rate³⁰ between those of SLM and WAAM. Furthermore, the subsequent heat accumulation and complex thermal cycles due to

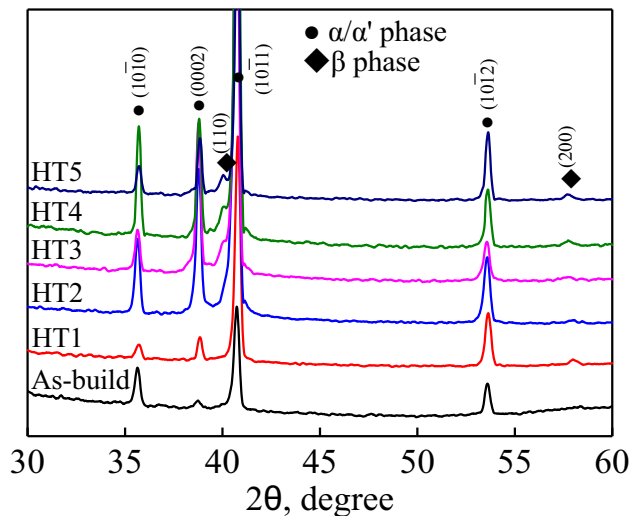


Fig. 3. XRD profiles of as-built and annealed Ti-6Al-4V.

the layer-by-layer deposition process can also affect the microstructure morphology.

Microstructure of Heat-Treated Alloy

Figure 4a, b, c, d, e, f, g, h, i and j presents microstructures annealed at different temperatures. It was reported that α' martensite in SLMed Ti-6Al-4V started to decompose at $\sim 400^\circ\text{C}$.³¹ After annealing at 690°C and 750°C for 2 h followed by FC, it can be observed that continuous α_{GB} locates at prior β grain boundary. Due to the lower diffusion driving force of atoms and slower solute redistribution rate at low temperature, α' martensite morphology can still be observed in prior β grains (Fig. 4a and c). The magnified microstructures in Fig. 4b and d show that a large amount of particle-like β phase and a small amount of thin rod-like β phase distribute at the boundary of α' martensite, which is an indication of the initiation of α' decomposition. Similar morphologies have been reported in Ti-6Al-4V alloy annealed at 730°C and 780°C for 2 h followed by FC.^{18,26} As the annealing temperature exceeds 800°C , the α' martensite morphology disappears and the microstructure shows a basket-weave structure (Fig. 4e, g, and i). The magnified microstructures in Fig. 4f, h, and j show that β phase presents continuous lamellar morphology. A similar transformation could also be found in Ref. 13. It can be observed from the XRD profiles that the intensity of (110) β phase peaks increases as the annealing temperature is increased, which implies an increasing amount of β phase.

Acicular α' martensite, formed during the rapid cooling, has the same crystal structure as α phase but is supersaturated by vanadium. The large lattice distortion due to the martensitic transformation results in enormous energy stored in the α' , which leads to instability. When the alloy is subjected to the thermal treatment, metastable α' will decompose into $\alpha + \beta$ phases as a result of the violent

diffusion of solute atoms. For this process, two mechanisms of martensitic decomposition have been proposed: (1) α phase takes the lead to nucleate heterogeneously along the martensite boundary and grow. Al diffuses into and V is expelled from the newly formed α phase. As time continues, this element partition effect becomes increasingly obvious, then the β phase forms at the α phase boundary;^{18,26,32} (2) V concentrates at the α' martensite boundary and the β phase nucleates and forms into particles or rods and α' martensite transforms into α phase as a consequence.^{33–35} In the present study, the latter seems more reasonable. Although the morphology of α' martensite remains essentially unchanged, more particle-like β and some rod-like β appears at the α' martensite boundary when annealed at 690°C (Fig. 4b). This indicates that α' martensite begins to decompose under the lead of the β generation. As the annealing temperature rises, more rod-like β appears. When the annealing temperature reaches 810°C (Fig. 4f), disconnected β particles and β rods connected to form continuous β phase and acicular α' transformed completely into α lamellae. Figure 4k, l, m and n shows schematic diagrams of β phase precipitation during the decomposition of α' martensite at different temperatures. The temperature is the most important factor for diffusion. Higher temperature could lead to more atomic thermal activation energy. In addition, the Gibbs free energy of hcp and bcc in Ti are equal at 800°C ³⁶ and the α' martensite in Ti-6Al-4V is unstable at high temperature and tends to decompose into $\alpha + \beta$ phase³³. When annealing at temperatures below 800°C , atoms can only diffuse over a short range, and the β phase nucleates and precipitates at α' boundary in a particle-like fashion. Increasing the temperature and prolonging the holding time could both cause the β phase to grow and interconnect, forming continuous rod-like or lamellar β phase.

Figure 5 shows the α lamellar width of as-built and annealed Ti-6Al-4V specimens. As reported in Ref. 18, the α lath width is primarily determined by the temperature and holding time for sub-transus heat treatment, being primarily determined by the cooling rate for heat treatment above β transus. In the present study, the width of the α lamellae increases obviously when the annealed temperature exceeds 810°C , and the lamellar width increases to $2.15 \pm 0.22 \mu\text{m}$ after annealing at 900°C .

The microstructure of solution- and aging-treated Ti-6Al-4V is illustrated in Fig. 6. The microstructure consists of short primary α lamellae (α_{p}) and ultrafine β transformation structure (β_{T} , α_{s} + β). The break-up of α_{p} and α_{GB} can be observed, which is the prelude to globularization.

A tremendous amount of work^{37–41} has been done on the globularization of α phase in titanium alloys, and the two most significant factors in the globularization process have been proposed to be deformation and heat treatment. The globularization

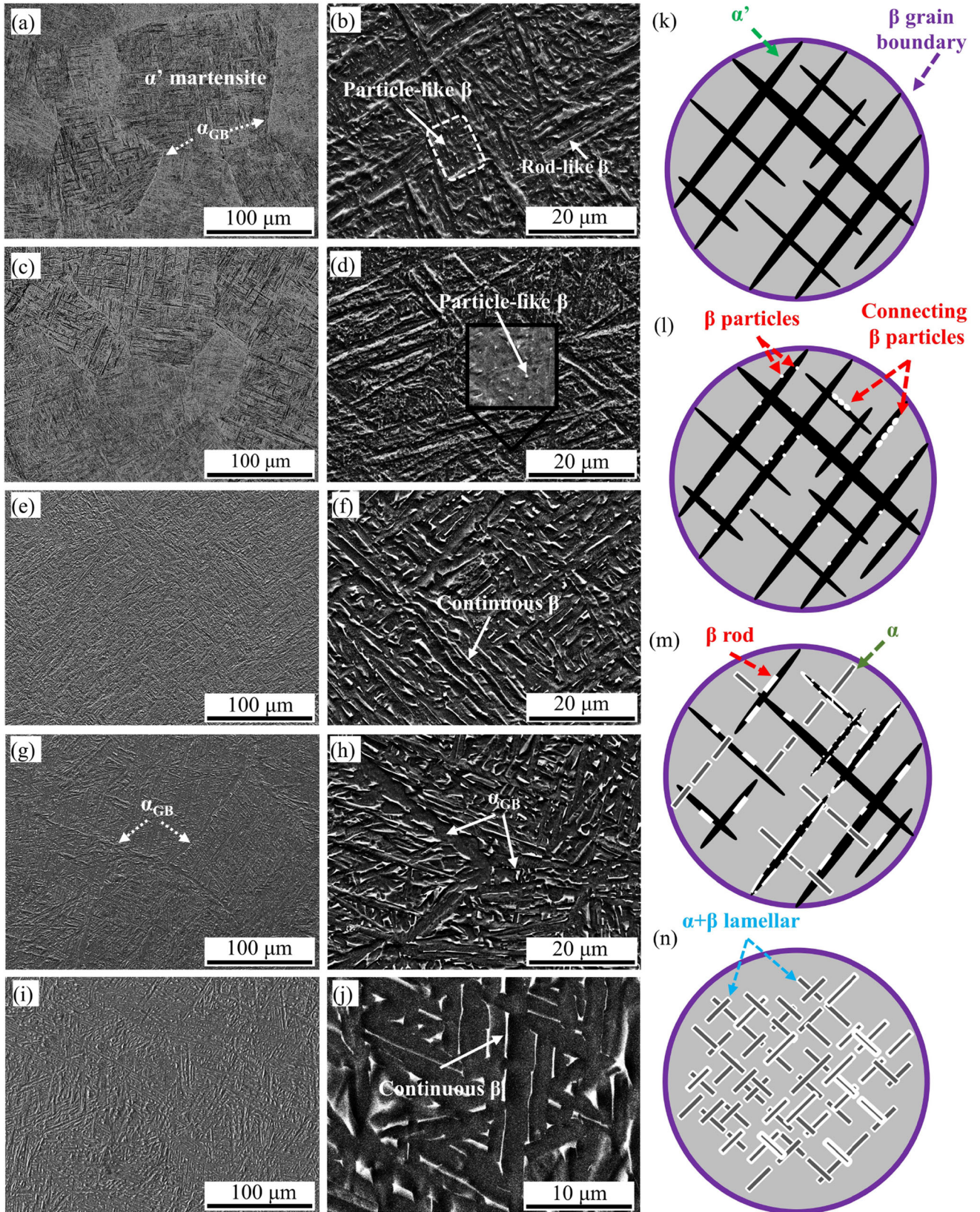


Fig. 4. SEM images of samples annealed at (a, b) 690°C/2 h/FC (HT1), (c, d) 750°C/2 h/FC (HT2), (e, f) 810°C/2 h/FC (HT3), (g, h) 870°C/2 h/FC (HT4), and (i, j) 900°C/2 h/FC (HT5). The α phase is dark, β phase is bright. (k–n) Schematic diagrams of β phase precipitation during decomposition of α' martensite at different temperatures. (k) Original α' martensite in prior β grain; (l) formation of β particles at α' boundary when heated at low temperature; (m) formation of β rods and α phase on heat treatment at higher temperature; (n) formation of $\alpha + \beta$ lamellar structure with α' completely decomposed.

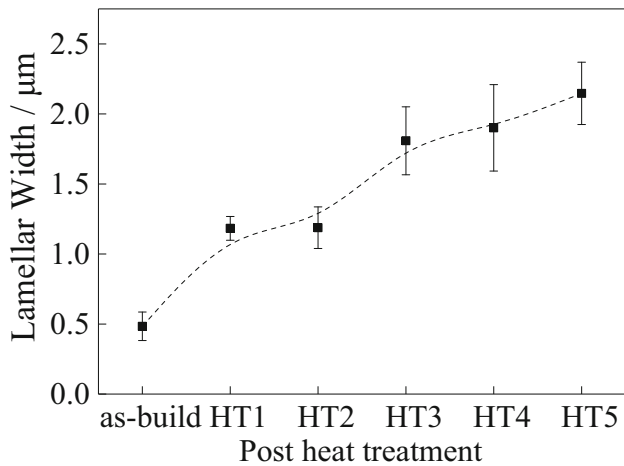


Fig. 5. Measured α lamellar width of as-built and annealed Ti-6Al-4V alloy.

process mentioned above can be divided into two stages: boundary splitting at the initial stage of heat treatment, and termination migration during the heat treatment.

Multiple thermal cycling and supersaturated α' cause large residual stress in the material during the deposition process, leaving the tangled dislocations in a high-energy state. It is noteworthy that Sabban et al.³⁸ obtained spheroidized α phase in SLMed Ti-6Al-4V through repeated thermal cycling close to but below the β transus temperature for as long as 24 h. For CAEBWAM, the thermal cycling is much more extensive than in SLM, and the samples have undergone repeated thermal cycling during the building process, similar to a thermal cycle treatment. This is why so many α lamellae break up after solution and aging treatment. As the heat treatment exceeds a certain duration, the dominant mechanism of break-up changes from boundary splitting to termination migration, and the demarcation point of these two processes is reported to be approximately 0.5 h to 1 h.⁴¹ Similar to boundary splitting, termination migration is a process of atomic diffusion, as well. The difference is that the driving force for termination migration is provided by the curvature difference at different sites of α plates. The higher the potential energy, the more intense the diffusion of atoms on the higher-curvature surface. The solute atoms diffuse from the termination with high curvature to the plane with low curvature, resulting in dissolution of the termination and further coarsening of the α plates. At the same time, more noncoherent interphase termination occurs due to the continuous boundary splitting, which makes the diffusion of solute atoms change from long- to short-range diffusion and accelerates the terminal migration, as shown by the dotted circle in Fig. 6a and c. In fact, termination migration is a phase transformation process for $\alpha \rightarrow \beta$ at the curving termination and $\beta \rightarrow \alpha$ at the flat interface.

Tensile Properties

In our previous study,²³ it was found that the anisotropy of the tensile properties in the X versus Z direction was weakened as a result of the formation of a large number of equiaxed β grains. Therefore, only X -oriented tensile samples were tested in the present study.

Figure 7 shows the tensile properties of CAEBWAMed Ti-6Al-4V after different post-heat treatments. After annealing at 690°C to 900°C, as the temperature was increased, the ultimate tensile strength (UTS) and yield strength (YS) decreased while the elongation (EL) increased. Note that no significant changes in the UTS or YS were observed between the lower temperatures of 690°C and 750°C. For Ti-6Al-4V after different heat treatments, the evolution of the microstructure often corresponds to the change in the properties.²⁶ As illustrated in Fig. 4a and c, α' martensite morphology could still be observed in prior β grains, thus similar microstructure leads to similar tensile performance. In addition, it can be seen in Fig. 5 that there was no significant increase in the lamellar width between HT1 and HT2. This means that the effective slip length of the dislocation does not increase. The slight increase in elongation can be interpreted as a reduction of the dislocation density, which leads to the release of residual stress during the partial decomposition of martensite, because severe stress concentration often results in early failure under loading. The residual α' martensite is a brittle phase with a high density of dislocations, which results in poor performance in accommodating strain. In addition, a large number of disordered dislocations around them could lead to stress concentration. As illustrated in Fig. 4e, f, g, h, i and j, α' martensite fully decomposed into $\alpha + \beta$ lamellae, and the residual stress was completely released during annealing at an elevated temperature above 800°C. Therefore, the ductility continues to increase, while the strength shows an opposite trend. As mentioned above, the ductility is related to the effective slip length of dislocation, which increases as the α lamellar width increases. It is worth noting that the α lamellar width increases sharply from $1.19 \pm 0.15 \mu\text{m}$ to $1.81 \pm 0.24 \mu\text{m}$ between HT2 and HT3, and continues to increase thereafter, which leads to an increase in the EL and a decrease in the strength, as well. Meanwhile, the results above are consistent with the Hall–Petch relationship.

After solution treatment at 940°C, the α_p lamellar width increases strongly. According to the Hall–Petch relationship, the tensile strength should be reduced due to the large slip length of dislocations. On the contrary, the UTS does not decrease but is higher than for HT5. This is because of the dispersion strengthening of α_s during the subsequent aging treatment when dislocations are pinned by the precipitated β_T phase (Fig. 6). Moreover, the aging process produced a small and narrow plastic

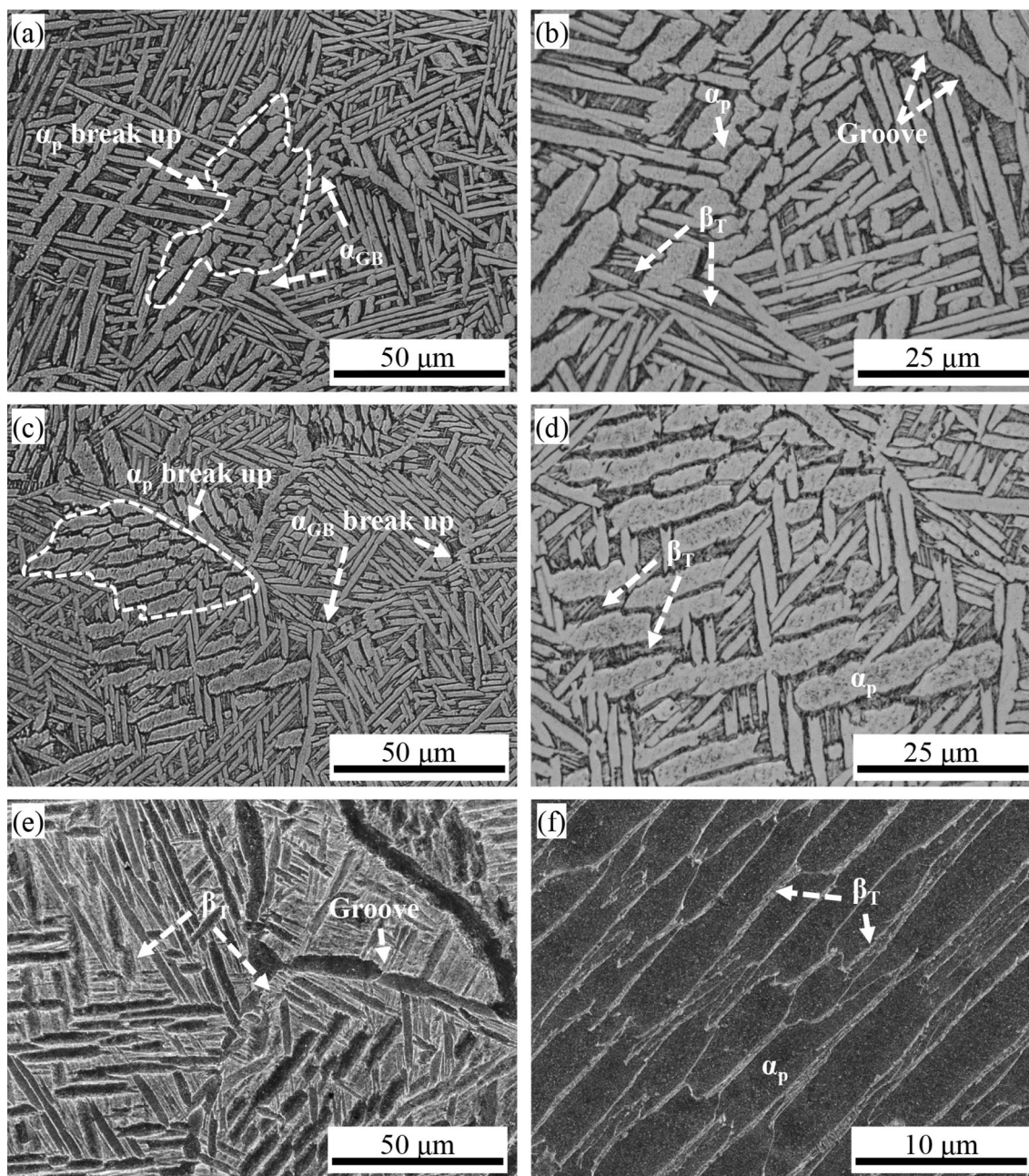


Fig. 6. Microstructures of solution- and aging-treated alloy: (a, b) 940°C/1 h/AC + 540°C/4 h/AC (HT6), (c, d) 940°C/1 h/AC + 560°C/4 h/AC (HT7), and (e, f) 960°C/1 h/AC + 560°C/4 h/AC (HT8).

region that required more energy for crack propagation⁴², so larger stress is needed to break the samples. The influence of α_{GB} on the ductility cannot be ignored either. During deformation, the α_{GB} acts as an obstacle that hinders transgranular movement of dislocations. Hence, the hindered dislocations pile up at the grain boundary and inhibit the migration of dislocations by back-stress, resulting in serious stress concentration.⁴³ Premature intergranular fracture often takes place along the prior β grain boundaries due to the early cracks that nucleate at stress concentration sites; similar fractures can be found in Refs. 44 and 45 After

solution treatment at elevated temperature, a large number of α_{GB} begin to break, as indicated by white arrows in Fig. 6, which may correspond to the increase in elongation.

Copmaring HT6 and HT7, although aging at different temperatures for 4 h, the effect on the tensile performance seems to be negligible. However, for the solid solution at a higher temperature for the same time, the tensile properties of HT8 show lower strength but the highest elongation of 19%. This may indicate that the effect of globularization on the tensile performance is the dominant factor rather than the precipitation of α_S .

Table I presents the room-temperature tensile results of the present study and other different AM methods for Ti-6Al-4V in different states. Compared with heat-treated Ti-6Al-4V fabricated by other manufacturing methods, the samples fabricated by this new technology showed excellent performance in all treatment situations. Among these, HT4 seems to be the most preferred post-heat treatment for this technology, eliminating the α' martensite completely and retaining the fine $\alpha + \beta$ lamellae, resulting in the optimal combination of high strength and superior elongation.

CONCLUSION

The effects of annealing treatments at different temperatures as well as solution and aging treatments on the microstructural evolution and tensile properties were investigated. Based on the results, the following conclusions can be drawn:

1. The as-built alloy was dominated by equiaxed prior β grains. The as-built alloy showed a mixed microstructure composed of large α' martensite and fine $\alpha + \beta$ lamellae. As the annealing temperature was increased, α' martensite decomposed into $\alpha + \beta$ phase and the α lamellar width increased, leading to increasing ductility and decreasing strength. After annealing at 690°C and 750°C, α' martensite decomposed partly and β phase precipitated at the boundary of α' martensite with particle and rod morphologies.
2. After annealing at 810°C, the coarsening of α lamellae and decomposition of martensite became stronger due to the faster diffusion rate of atoms. α' martensite decomposed completely into $\alpha + \beta$ lamellar, and the lamellar width increased to 1.81 μm .
3. At increased annealing temperature, both the ultimate tensile strength and yield strength showed a declining trend, reaching minimum values of 947.5 MPa and 835 MPa at 900°C, while the ductility followed the opposite trend. Ti-6Al-4V annealing at 870°C (HT4) possessed the best combination of superior strength (992.5 MPa for UTS and 887.5 MPa for YS) with high elongation (17.25%).

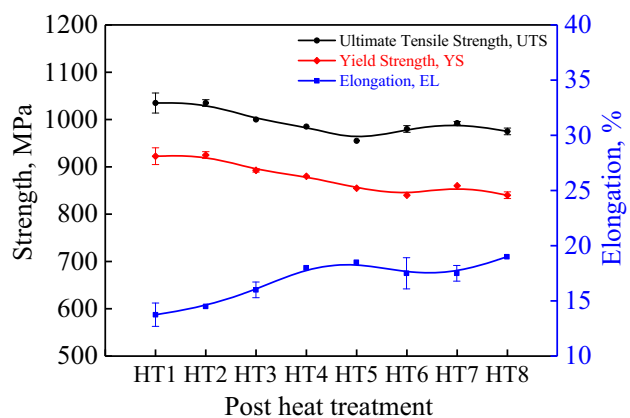


Fig. 7. Tensile properties of CAEBWAMed Ti-6Al-4V after different post-heat treatments.

Table I. Summary of tensile properties with different AMed Ti-6Al-4V samples (WQ, water quenching) 18:20:24:25:37:38:46.

Manufacturing Method	Heat Treatment	Ultimate Tensile Strength (MPa)	Yield Strength (MPa)	Elongation (%)
CAEBWAM	HT1	1035	922.5	13.8
CAEBWAM	HT2	1035	925	14.5
CAEBWAM	HT3	1000	882.5	16
CAEBWAM	HT4	985	880	18
CAEBWAM	HT5	955	855	18.5
SLM24	800°C/2 h/FC	945	869	18
SLM18	850°C/2 h/FC	1004	955	12.84
SLM25	800°C/2 h/FC	1223	996	7
	900°C/2 h/FC	945	869	18
WAAM46	1200 K/2 h/FC	810	721	11.5
WAAM20	850°C/2 h/AC	845	734	13.6
CAEBWAM	HT6	980	840	17.5
CAEBWAM	HT7	992.5	860	17.5
CAEBWAM	HT8	975	840	19
SLM38	Thermal cycle between 975°C and 875°C/24 h/AC	1017	865	18
LSF37	980°C/1 h/FC, 920°C/1 h/AC, 600°C/4 h/AC	905	829.3	25.1
WAAM20	930°C/1 h/WQ, 800°C/2 h/AC	886	847	12.2

4. After solid-solution treatment at elevated temperature, a large number of α_{GB} and α plates began to break up and even spheroidize by infiltration of β phase. The precipitation of α_S compensated for the decrease in strength due to the increase of the lamellar width. Elongation reached a maximum of 19% in the HT8 state.

ACKNOWLEDGEMENTS

This research is supported by Frontier and Key Projects of the Chinese Academy of Sciences (QYZDJ-SSW-JSC031-01) and an internal funding source from University of Shanghai for Science and Technology.

CONFLICT OF INTEREST

On behalf of all authors, the corresponding author states that there are no conflicts of interest.

REFERENCES

1. G. Lütjering, and J.C. Williams, *Titanium*, 2nd edn. (Springer, Berlin Heidelberg, 2007), pp 1–442.
2. R. Biswal, X. Zhang, A.K. Syed, M. Awd, J. Ding, F. Walther, and S. Williams, *Int. J. Fatigue* 122, 208. (2019).
3. P.J. Arrazola, A. Garay, L.M. Iriarte, M. Armendia, S. Marya, and F. Le Maitre, *J. Mater. Process. Technol.* 209, 2223. (2009).
4. J.K. Zhang, X.Y. Wang, S. Paddea, and X. Zhang, *Mater. Des.* 90, 551. (2016).
5. G. Lütjering, *Mater. Sci. Eng., A*, 243, 32 (1998).
6. A. Manoj, M.A. Rao, M.M. Basha, S.M. Basha, and M.R. Sankar, *Mater. Today. Proc* 26, 2608. (2020).
7. F.D. Wang, S. Williams, P. Colegrove, and A.A. Antonysamy, *Metall. Mater. Trans. A* 44, 968. (2012).
8. L. Thijs, F. Verhaeghe, T. Craeghs, J.V. Humbeeck, and J.P. Kruth, *Acta Mater.* 58, 3303. (2010).
9. M. Simonelli, Y.Y. Tse, and C. Tuck, *Mater. Sci. Eng. A* 616, 1. (2014).
10. X.Z. Shi, S.Y. Ma, C.M. Liu, Q.R. Wu, J.P. Lu, Y.D. Liu, and W.T. Shi, *Mater. Sci. Eng. A* 684, 196. (2017).
11. T. Sun, Y. Liu, S. J. Li and J. P. Li, *Acta Metall. Sin.* (Engl. Lett.), 32, 869 (2019).
12. N. Li, S. Huang, G.D. Zhang, R.Y. Qin, W. Liu, H.P. Xiong, G.Q. Shi, and J. Blackburn, *J. Mater. Sci. Technol.* 35, 242. (2019).
13. S. Cao, Q.D. Hu, A.J. Huang, Z.E. Chen, M. Sun, J.H. Zhang, C.X. Fu, Q.B. Jia, C.V.S. Lim, R.R. Boyer, Y. Yang, and X.H. Wu, *J. Mater. Sci. Technol.* 35, 1578. (2019).
14. J. C. Wang, Y. J. Liu, P. Qin, S. X. Liang, T. B. Sercombe and L. C. Zhang, *Mater. Sci. Eng., A*, 760, 214 (2019).
15. J.C. Wang, Y.J. Liu, C.D. Rabadia, S.X. Liang, T.B. Sercombe, and L.C. Zhang, *J. Mater. Sci. Technol.* 61, 221. (2021).
16. W.E. Frazier, *J. Mater. Eng. Perform.* 23, 1917. (2014).
17. J. Wang, X. Lin, J.T. Wang, H.O. Yang, Y.H. Zhou, C. Wang, Q.G. Li, and W.D. Huang, *J. Alloys Compd.* 768, 97. (2018).
18. B. Vrancken, L. Thijs, J.-P. Kruth, and J. Van Humbeeck, *J. Alloys Compd.* 541, 177. (2012).
19. S.Q. Wu, Y.J. Lu, Y.L. Gan, T.T. Huang, C.Q. Zhao, J.J. Lin, S. Guo, and J.X. Lin, *J. Alloys Compd.* 672, 643. (2016).
20. J. Wang, X. Lin, J. Q. Li, A. T. Xue, F. G. Liu, W. D. Huang and E. Q. Liang, *Mater. Sci. Eng., A*, 772, 138703 (2020).
21. K. Zhang, X. Tian, M. Bermingham, J. Rao, Q. Jia, Y. Zhu, X. Wu, S. Cao and A. Huang, *Mater. Des.*, 184, 108191 (2019).
22. D. Kovalchuk, and O. Ivasishin, *Profile electron beam 3-D metal printing // Additive Manufacturing for the Aerospace Industry*, 1st edn. (Elsevier, Amstel Dam, 2019), pp 213–233.
23. J. H. Zhang, Y. Yang, S. Cao, Z. Q. Cao, D. Kovalchuk, S. Q. Wu, E. Q. Liang, X. Zhang, W. Chen, F. Wu and A. J. Huang, *Acta Metall. Sin.* (Engl. Lett.), 33, 1311 (2020).
24. S. Cao, R.K. Chu, X.G. Zhou, K. Yang, Q.B. Jia, C.V.S. Lim, A.J. Huang, and X.H. Wu, *J. Alloys Compd.* 744, 357. (2018).
25. X.C. Yan, S. Yin, C.Y. Chen, C.J. Huang, R. Bolot, R. Lupoi, M. Kuang, W.Y. Ma, C. Coddet, H.L. Liao, and M. Liu, *J. Alloys Compd.* 764, 1056. (2018).
26. X.Y. Zhang, G. Fang, S. Leeflang, A.J. Böttger, A.A. Zadpoor, and J. Zhou, *J. Alloys Compd.* 735, 1562. (2018).
27. J.Q. Xu, J. Zhu, J.K. Fan, Q. Zhou, Y. Peng, and S. Guo, *Vacuum* 167, 364. (2019).
28. J. Wang, X. Lin, M. Wang, J. Q. Li, C. Wang and W. D. Huang, *Mater. Sci. Eng., A*, 776, 139020 (2020).
29. P. Wanjara, K. Watanabe, C. de Formanoir, Q. Yang, C. Bescond, S. Godet, M. Brochu, K. Nezaki, J. Gholipour, and P. Patnaik, *Adv. Mater. 9Sci. Eng* 2019, 1. (2019).
30. J.J. Lin, Y.H. Lv, Y.X. Liu, Z. Sun, K.B. Wang, Z.G. Li, Y.X. Wu, and B.S. Xu, *J. Mech. Behav. Biomed.* 69, 19. (2017).
31. W. Xu, M. Brandt, S. Sun, J. Elambasseril, Q. Liu, K. Latham, K. Xia, and M. Qian, *Acta Mater.* 85, 74. (2015).
32. F.X.G. Mur, D. Rodriguez, and J.A. Planell, *J. Alloys Compd.* 234, 287. (1996).
33. E. Sallica-Leva, R. Caram, A.L. Jardini, and J.B. Fogagnolo, *J. Mech. Behav. Biomed.* 54, 149. (2016).
34. Q. Chao, P.D. Hodgson, and H. Beladi, *Metall. Mater. Trans. A* 45, 2659. (2014).
35. P. Barriobero-Vila, V. Biancardi Oliveira, S. Schwarz, T. Buslaps and G. Requena, *Acta Mater.*, 135, 132 (2017).
36. S.L. Lu, M. Qian, H.P. Tang, M. Yan, J. Wang, and D.H. StJohn, *Acta Mater.* 104, 303. (2016).
37. Z. Zhao, J. Chen, H. Tan, G.H. Zhang, X. Lin, and W.D. Huang, *Scripta Mater.* 146, 187. (2018).
38. R. Sabban, S. Bahl, K. Chatterjee, and S. Suwas, *Acta Mater.* 162, 239. (2019).
39. N. Stefansson, and S.L.S. Tin, *Metall. Mater. Trans. A* 34A, 691. (2003).
40. K. Chen, J. Luo, W. C. Han and M. Q. Li, *J. Alloys Compd.*, 848, 156141 (2020).
41. J.W. Xu, W.D. Zeng, H.Y. Ma, and D.D. Zhou, *J. Alloys Compd.* 736, 99. (2018).
42. L. Ren, W.L. Xiao, W.Z. Han, C.L. Ma, and L. Zhou, *Mater. Charact.* 144, 1. (2018).
43. C. M. Liu, Y. Lu, X. J. Tian and D. Liu, *Mater. Sci. Eng., A*, 661, 145 (2016).
44. P. Åkerfeldt, M.-L. Antti and R. Pederson, *Mater. Sci. Eng., A*, 674, 428 (2016).
45. B.E. Carroll, T.A. Palmer, and A.M. Beese, *Acta Mater.* 87, 309 (2015).
46. M.J. Bermingham, L. Nicastro, D. Kent, Y. Chen, and M.S. Dargusch, *J. Alloys Compd.* 753, 247. (2018).

Publisher's Note Springer Nature remains neutral with regard to jurisdictional claims in published maps and institutional affiliations.